

# Shocks, illumination cones and intrinsic gas structures in the extreme radio galaxy 3C 265

C. Solórzano-Iñarrea<sup>1,2★†</sup>, C. N. Tadhunter<sup>1</sup> and J. Bland-Hawthorn<sup>3</sup>

<sup>1</sup>*Department of Physics and Astronomy, University of Sheffield, Sheffield, S3 7RH, UK*

<sup>2</sup>*Department of Physics and Astronomy, University of Leeds, Leeds, LS2 9JT, UK*

<sup>3</sup>*Anglo-Australian Observatory, PO Box 296, Epping, NSW 2121, Australia*

1 February 2008

## ABSTRACT

We present deep, narrow-band and continuum images of the powerful high-redshift radio galaxy 3C 265 ( $z=0.811$ ), taken with the TAURUS Tunable Filter on the William Herschel Telescope, together with detailed long-slit spectroscopic observations along the axis defined by the UV/optical emission elongation. The deep images reveal the existence of cones in the ionization structure of 3C 265 within  $\sim 7$  arcsec (58 kpc) of the nucleus, where the emission-line structure is not observed to be closely aligned with the radio axis. This indicates that anisotropic illumination from the central active nucleus dominates on a small scale. In contrast, at larger distances ( $\gtrsim 10$  arcsec; 80 kpc) from the nucleus, low-ionization emission gas is closely aligned with the radio axis, suggesting that jet-cloud interactions may become the dominant mechanism in the line-emitting gas on a larger scale. Moreover, the presence of a high-velocity cloud at 2.5 arcsec from the nucleus, close to the radio axis, indicates that even close to the nucleus ( $\sim 20$  kpc) jet-induced shocks have an important kinematic effect. However, spectroscopic analysis of this region reveals that the ionization state of the high-velocity gas is similar to or higher than that of the surroundings, which is opposite to what we would expect for a cloud that has been compressed and accelerated by jet-induced shocks.

Our images show that, while on a large scale the low-ionization emission-line structures are aligned with the radio axis, on a smaller scale, where AGN-photoionization dominates, the highest surface-brightness structure is aligned with the closest companion galaxy (misaligned with the radio axis). This suggests that much of the emission-line structure reflects the intrinsic gas distribution, rather than the ionization pattern imprinted by the radio jets or by illumination from the central AGN.

Overall, our results underline the need for a variety of mechanisms to explain the properties of the extended emission-line gas in the haloes of radio galaxies.

**Key words:** galaxies: active — galaxies: individual: 3C 265 — galaxies: structure — galaxies: jets — galaxies: kinematics and dynamics.

## 1 INTRODUCTION

One of the most important issues concerning radio galaxies is the dominant ionization mechanism of the extended line-emitting gas in these sources. These emission-line regions extend large distances from the nucleus, and provide important information about both the origin of the activity and the origin of the extended gas. However, the main

physical processes affecting the properties of the extended emission-line regions (EELR) are not fully understood.

The two most accepted models are: a) photoionization by the central active galactic nucleus (AGN), and b) shock-ionization by the interactions between the radio- and line-emitting structures, the so-called ‘jet-cloud interaction’ model. (See Tadhunter 2001 for a review.)

While most (but not all) low-redshift radio galaxies appear to be consistent with AGN-photoionization, as we move to higher redshifts there is increasing evidence for shocks. Many distant radio galaxies present highly disturbed kinematics, mostly along the radio axis (McCarthy, Baum &

★ E-mail: csi@roe.ac.uk

† Present address: Institute for Astronomy, University of Edinburgh, Royal Observatory, Edinburgh, EH9 3HJ, UK.

Spinrad 1996), and highly collimated optical/UV structures aligned along the radio axis (McCarthy et al. 1987; Best, Longair & Röttgering 1996).

In addition to the general alignments, detailed study of a sample of  $z \sim 1$  radio galaxies has revealed a strong evolution of the emission-line properties with radio size (Best, Röttgering & Longair 2000): the emission-line regions of small radio sources show disturbed kinematics and emission-line ratios in agreement with shock predictions; while larger radio sources appear more quiescent and present emission-line ratios consistent with AGN-photoionization. However, recent kinematic studies of a sample of  $z \lesssim 0.8$  radio galaxies have provided evidence that shocks have an important effect on the emission-line properties in all sources, even those in which the radio structures are on a much larger scale than the emission-line structures (Solórzano-Iñarrea, Tadhunter & Axon 2001).

It seems clear that a combination of both AGN-photoionization and shock-ionization is required to explain the observed properties in the emission-line regions of radio galaxies over the whole range of redshifts and radio power. However, the balance between these mechanisms is not yet clear. In order to address this issue, we require complete maps of both the kinematics and ionization structure in the extended haloes of radio galaxies, and not only spectroscopic studies along a preferred direction (e.g. radio axis), which offer a limited view of the properties of the emission-line gas in these sources. To this end, in this paper we present deep emission-line imaging of the powerful high-redshift radio galaxy 3C 265, taken with the TAURUS Tunable Filter (TTF), which are aimed at determining the dominant physical mechanisms. While the published ground-based images of high-redshift radio galaxies are relatively shallow, and the higher-resolution Hubble Space Telescope (HST) images are insensitive to low-surface brightness structures, the TTF is sensitive enough to detect faint structures in the galaxy halo. In addition, the TTF also allows a narrow bandpass, which, for our observations, was tuned to observe the high-velocity gas (Tadhunter 1991), as well as the unshifted component, therefore permitting a two-dimensional kinematic analysis of the galaxy.

To supplement the TTF images, we also present long-slit spectroscopic observations of 3C 265 taken along PA  $145^\circ$ , the axis defined by the UV/optical emission elongation. Preliminary results of these observations were presented in Tadhunter (1991). Here we present a more detailed analysis.

Throughout this paper a Hubble constant of  $H_0 = 50 \text{ km s}^{-1} \text{ Mpc}^{-1}$  and a density parameter of  $\Omega_0 = 1$  are assumed, resulting in an angular scale of  $8.25 \text{ kpc arcsec}^{-1}$  for 3C 265.

## 2 PREVIOUS OBSERVATIONS OF 3C 265

3C 265 is a large (78 arcsec; 643 kpc) radio source, with a redshift  $z=0.811$  (see radio map in Fernini et al. 1993). Its extreme emission-line luminosity — an order of magnitude brighter than other radio galaxies at the same redshift (McCarthy 1988) — makes 3C 265 unique for the study of emission-line properties in distant radio galaxies.

Unlike other powerful high- $z$  radio galaxies (e.g.

3C 368), 3C 265 is not a good example of the alignment effect. The rest-frame UV emission is misaligned by approximately  $35^\circ$  relative to the radio axis. Nevertheless, this misalignment is still consistent with the large half-opening angles ( $\sim 45^\circ - 60^\circ$ ) for the ionization cones predicted by the unified schemes for radio sources (e.g. Barthel 1989).

3C 265 presents strongly polarized rest-frame UV continuum and broad MgII  $\lambda\lambda 2799$  emission, with the polarization position angle oriented perpendicular to the extended UV emission rather than to the radio axis (Jannuzi & Elston 1991; Dey & Spinrad 1996; di Serego Alighieri et al. 1996). This provides strong evidence for the extended gas being illuminated by a powerful hidden quasar in the nucleus of 3C 265. In addition, a more recent analysis of the ionization state of the emission-line gas in 3C 265 shows that the near-UV emission-line ratios are consistent with AGN-photoionization (Best et al. 2000). Therefore, at first sight, 3C 265 appears to be one of the best high redshift examples of an object dominated by AGN-photoionization.

However, Tadhunter (1991) reports the discovery of high-velocity gas in the extended emission-line region of 3C 265. The presence of this high-velocity gas suggests that jet-induced shocks may also contribute to the ionization of the ambient gas at some level.

## 3 OBSERVATIONS, DATA REDUCTION AND ANALYSIS

### 3.1 Optical spectroscopy

Long-slit spectroscopic observations were carried out on the night 23/01/91, using the red arm of the ISIS double spectrograph on the 4.2m William Herschel Telescope (WHT) on La Palma (Spain). The EEV2 CCD detector was used, giving a pixel scale of  $0.327 \text{ arcsec/pix}$ . The  $2.16 \text{ arcsec}$  slit was oriented along the axis defined by the elongation of the optical/UV emission (PA  $145^\circ$ ), roughly perpendicular to the observed B-band polarization position angle (Jannuzi & Elston 1991), and misaligned by  $\sim 35^\circ$  relative to the radio axis. Two individual spectra were coadded to produce a single spectrum with a exposure time of 3600 seconds. Details of the observations are presented in Tadhunter (1991).

The reduction of the long-slit spectra was performed using the IRAF software package, following the usual steps: bias-subtraction, cosmic-ray removal, flat-fielding, wavelength calibration, atmospheric extinction correction, flux calibration and sky subtraction. A relative flux calibration error of  $\sim 9\%$  across the wavelength range was found by comparing different spectrophotometric standard star observations. After the basic reduction procedure, the two-dimensional spectra were corrected for any distortion along the spectral direction, using the Starlink FIGARO package. Finally, the spectra were shifted to the rest frame of the galaxy before the analysis. Then, the extracted one-dimensional spectra were analysed using the Starlink DIPSO spectral analysis package. Gaussians were fitted to the emission-line profiles. The measured linewidths were corrected for the spectral resolution of the instrument, which was derived using the night-sky and arc lines, and found to be  $15.60 \pm 0.16 \text{ \AA}$ . Since the airmass during the observations of 3C 265 was 1.03, the effects of differential atmospheric refraction can be neglected. The data have not been corrected

	Blocking Filter $\lambda_c(\text{\AA})/\Delta\lambda(\text{\AA})$	Etalon $\lambda_c(\text{\AA})/\Delta\lambda(\text{\AA})$	$t_{exp}$ (s)	Surface Brightness Limit ( $\text{erg cm}^{-2} \text{ s}^{-1} \text{ arcsec}^{-2}$ )	Seeing (FWHM) (arcsec)
Continuum	8122/330	—	2×900	$\sim 3 \times 10^{-17}$ (*)	1.17±0.10
[OII] low-vel.	6682/210	6742/20	2×900	$\sim 1 \times 10^{-17}$	1.16±0.05
[OII] high-vel.	6682/210	6769/20	900	$\sim 1.6 \times 10^{-17}$	1.20±0.06
[OIII] low-vel.	9094/400	9052/36	2×900	$\sim 1.6 \times 10^{-17}$	1.18±0.06
[OIII] high-vel.	9094/400	9090/36	2×900	$\sim 3 \times 10^{-17}$	1.07±0.09

**Table 1.** Log of the TTF imaging observations for 3C 265. The second and third columns give the central wavelength/bandwidths for the blocking filters and the etalon, respectively. (\*)Total surface brightness integrated across the bandwidth of the broad-band filter (330Å).

for Galactic reddening, given that 3C 265 does not have a low Galactic latitude, and therefore the extinction due to dust in our Galaxy is not large [E(B-V)=0.023 mag; taken from NASA/IPAC Extragalactic Database (NED)].

### 3.2 Optical imaging

Emission-line and continuum observations of 3C 265 were taken on the night 22/01/98 using the TTF on the WHT on La Palma (Spain). A full description of the TTF is given in Bland-Hawthorn & Jones (1998a,b). Use of the f/2 camera of TAURUS and the Tek5 CCD detector resulted in a pixel scale of 0.557 arcsec/pix. A log of the observations is presented in Table 1. The etalon was tuned to the redshifted wavelengths of the low- and high-velocity components of both [OII]  $\lambda\lambda 3727$  and [OIII]  $\lambda 5007$  emission lines (see Tadhunter 1991 and Section 4.2.2 for details of the shifted components). Observations of the spectrophotometric standard star SP1337+705 and dome flats were taken at each wavelength setting. Estimates of the seeing FWHM were derived by fitting the spatial profiles of several stars in the field. No significant variations in the seeing were found between the different filter observations (see Table 1 for details).

The reduction of the TTF images was performed using IRAF and following the usual steps. After subtracting the bias (using the overscan region), the images were divided by the corresponding normalized flat-field frame, and cosmic rays were manually removed using the task IMEDIT. The different filter images were registered to a reference image (chosen to be that with the lowest airmass) to an accuracy of better than 0.1 pixels, using several stars in the frames (task IMALIGN). Those images taken with the same wavelength setting were coadded together. The resulting frames were corrected for atmospheric extinction, flux-calibrated and sky-subtracted. Because only one spectrophotometric standard star was observed during the 3C 265 observations, absolute flux calibration errors could not be estimated directly from the TTF images. To estimate the uncertainty in the flux calibration, we compared the reduced TTF images with the long-slit spectra along PA 145°, by simulating the position and width of the slit on the TTF frames. It was found that the [OII]/[OIII] line ratio obtained from the TTF images agreed with that derived from the long-slit spectra to within  $\pm 15$  % for radii less than 7 arcsec from the nu-

cleus, increasing to  $\pm 40$  % at distances of 7 to 10 arcsec from the nucleus. The surface brightness of the faintest structures visible in the images is given in Table 1.

## 4 RESULTS

### 4.1 Optical spectroscopy

#### 4.1.1 Emission-line kinematics

Kinematic studies of the line-emitting gas in 3C 265, based on long-slit spectroscopic observations (e.g. Dey & Spinrad 1996), show an ordered velocity profile with small velocity shifts ( $\Delta v \lesssim 300 \text{ km s}^{-1}$ ) relative to the nucleus, at least for the strongest emission-line components. This is consistent with gravitational motions in the potential of a single galaxy (Tadhunter, Fosbury & Quinn 1989; Baum, Heckman & van Breugel 1990).

Our reanalysis of the data presented in Tadhunter (1991) shows that the emission-line profiles can be fitted by single Gaussians in the north-western EELR, but in the nucleus and south-eastern EELR the profiles are more complex (see Fig. 1). The observed broad wings to the [OIII]  $\lambda\lambda 4959, 5007$  profiles in these regions show the existence of an underlying broad component in addition to the narrow component present in the nucleus and the two SE regions, as well as a high-velocity narrow component which is strongest in the SE-1 EELR — region studied by Tadhunter (1991). In Fig. 2 we show the [OIII] emission-line profiles (solid line) of the SE-1 region where the split components are observed, corresponding to a  $1.63 \times 2.16 \text{ arcsec}^2$  aperture centred at 1.5 arcsec south-east of the continuum centroid. Initially, a two-component Gaussian fit for each line of the doublet was considered, but the emission-line profiles could not be reproduced by this fit. Thus, a three-component Gaussian fit was considered (dot-dashed-dot) to fit the red broad wing seen in the [OIII] line, suggestive of the existence of an underlying broad component. The total fit is indicated by a dashed line. At the location of the splitting, this best fit consists of a blue-shifted low-velocity component at  $-222 \pm 3 \text{ km s}^{-1}$ , a red-shifted high-velocity component at  $+800 \pm 11 \text{ km s}^{-1}$ , and a very broad red-shifted underlying component with a velocity of  $+500 \pm 100 \text{ km s}^{-1}$  and a linewidth of  $2000 \pm 180 \text{ km s}^{-1}$  (FWHM). This provides

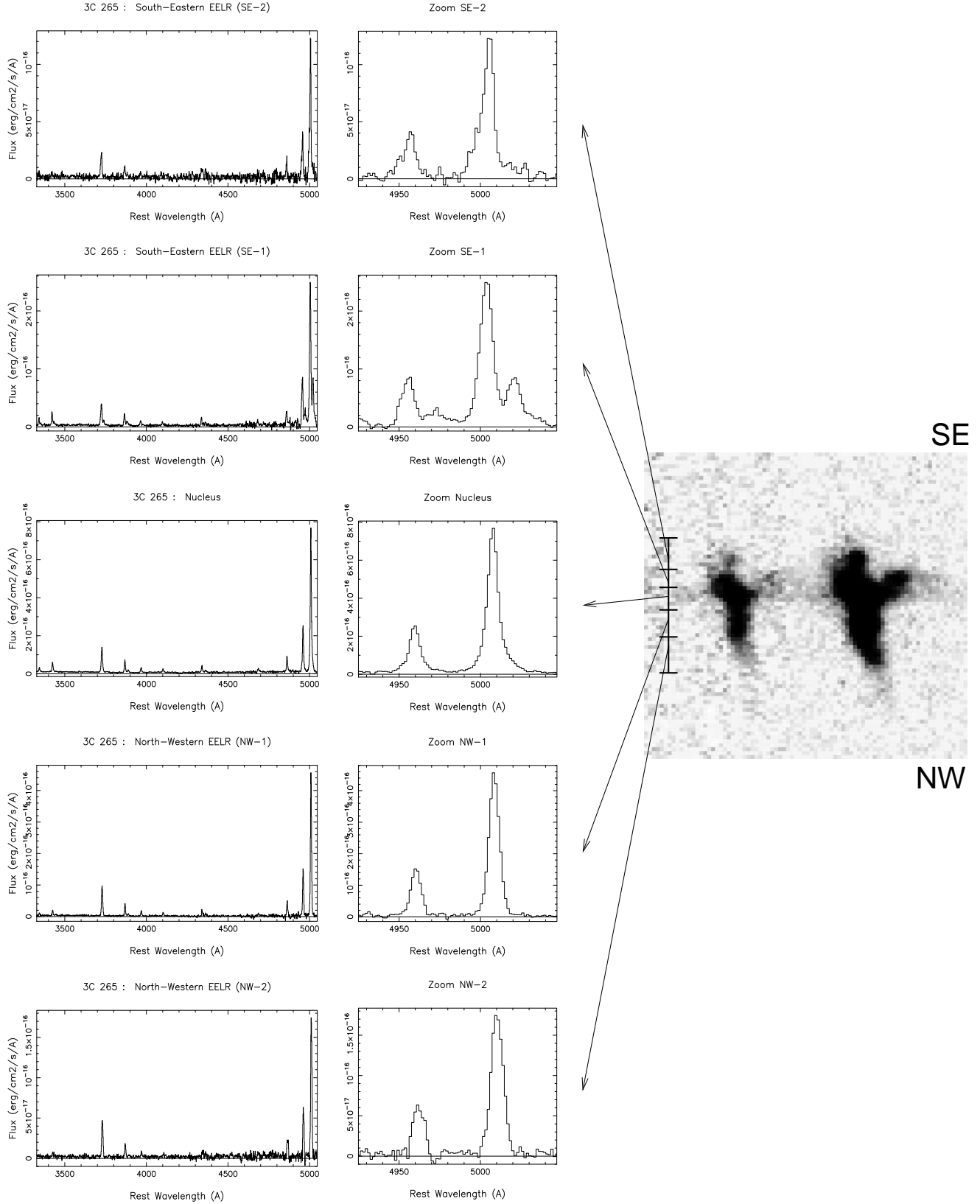


**Figure 1.** Integrated spectra of the different regions in 3C 265, together with a zoom of the [OIII] doublet, and 2-D spectrum showing the doublet [OIII] $\lambda\lambda 4959, 5007$  (4925 – 5047 Å, 25.5 arcsec along the PA 145° slit).

Line	SE-2 EELR (3''.8 SE)	SE-1 EELR (1''.5 SE)		Nucleus (0''.3 NW)	NW-1 EELR (2''.4 NW)	NW-2 EELR (5''.0 NW)
		low-vel.	high-vel.			
[NeV] $\lambda$ 3346 .....	—	0.27 $\pm$ 0.04	0.40 $\pm$ 0.15	0.24 $\pm$ 0.02	0.11 $\pm$ 0.02	—
[NeV] $\lambda$ 3426 .....	< 0.37	0.75 $\pm$ 0.11	1.11 $\pm$ 0.43	0.67 $\pm$ 0.04	0.31 $\pm$ 0.03	< 0.21
[OII] $\lambda$ 3727 .....	2.20 $\pm$ 0.46	1.85 $\pm$ 0.19	1.18 $\pm$ 0.36	2.01 $\pm$ 0.10	2.24 $\pm$ 0.17	2.16 $\pm$ 0.30
[NeIII] $\lambda$ 3869 .....	0.94 $\pm$ 0.21	0.86 $\pm$ 0.10	0.99 $\pm$ 0.38	0.77 $\pm$ 0.04	0.77 $\pm$ 0.06	0.64 $\pm$ 0.09
H8+HeI 3886 .....	0.27 $\pm$ 0.10	—	—	0.21 $\pm$ 0.03	0.15 $\pm$ 0.03	0.12 $\pm$ 0.04
[NeIII] $\lambda$ 3967 .....	0.30 $\pm$ 0.07	0.27 $\pm$ 0.03	0.31 $\pm$ 0.12	0.24 $\pm$ 0.02	0.24 $\pm$ 0.02	0.20 $\pm$ 0.03
H $\delta$ .....	—	0.23 $\pm$ 0.05	—	0.24 $\pm$ 0.02	0.26 $\pm$ 0.03	0.16 $\pm$ 0.05
H $\gamma$ .....	—	0.49 $\pm$ 0.07	—	0.45 $\pm$ 0.03	0.37 $\pm$ 0.04	0.37 $\pm$ 0.09
[OIII] $\lambda$ 4363 .....	—	0.24 $\pm$ 0.05	—	0.20 $\pm$ 0.02	0.17 $\pm$ 0.03	0.25 $\pm$ 0.07
HeII $\lambda$ 4686 .....	—	0.32 $\pm$ 0.07	—	0.27 $\pm$ 0.04	0.17 $\pm$ 0.05	—
H $\beta$ .....	1.00 $\pm$ 0.21	1.00 $\pm$ 0.11	1.00 $\pm$ 0.29	1.00 $\pm$ 0.05	1.00 $\pm$ 0.08	1.00 $\pm$ 0.14
[OIII] $\lambda$ 4959 .....	3.85 $\pm$ 0.88	3.62 $\pm$ 0.40	2.74 $\pm$ 0.86	3.54 $\pm$ 0.23	3.16 $\pm$ 0.25	2.44 $\pm$ 0.36
[OIII] $\lambda$ 5007 .....	12.57 $\pm$ 2.66	10.86 $\pm$ 1.19	8.21 $\pm$ 2.58	11.51 $\pm$ 0.61	9.88 $\pm$ 0.76	7.88 $\pm$ 1.10
<hr/>						
H $\beta$ flux ( $10^{-16}$ erg cm $^{-2}$ s $^{-1}$ )	1.76 $\pm$ 0.36	3.71 $\pm$ 0.39	1.12 $\pm$ 0.33	11.50 $\pm$ 0.58	6.69 $\pm$ 0.51	3.73 $\pm$ 0.52
<hr/>						
[OIII] $\lambda$ 5007 Velocity (km s $^{-1}$ )	-90 $\pm$ 8 (*)	-222 $\pm$ 3	+800 $\pm$ 11	+10 $\pm$ 2 (*)	+61 $\pm$ 2	+176 $\pm$ 5

**Table 2.** Emission-line fluxes of 3C 265, including the south-eastern EELR ‘SE-2’ ( $2.94 \times 2.16$  arcsec $^2$  aperture centred at 3.8 arcsec SE of the continuum centroid), the south-eastern EELR ‘SE-1’ ( $1.63 \times 2.16$  arcsec $^2$  aperture centred at 1.5 arcsec SE of the continuum centroid), the nucleus ( $1.96 \times 2.16$  arcsec $^2$  aperture centred at 0.3 arcsec NW of the continuum centroid), the north-western EELR ‘NW-1’ ( $2.29 \times 2.16$  arcsec $^2$  aperture centred at 2.4 arcsec NW of the continuum centroid) and the north-western EELR ‘NW-2’ ( $2.94 \times 2.16$  arcsec $^2$  aperture centred at 5.0 arcsec NW of the continuum centroid). The velocity of the [OIII] $\lambda$ 5007 emission-line for each aperture with respect to the velocity at the continuum centroid is also given. (\*) These velocities correspond to the main, narrow component of the fit.

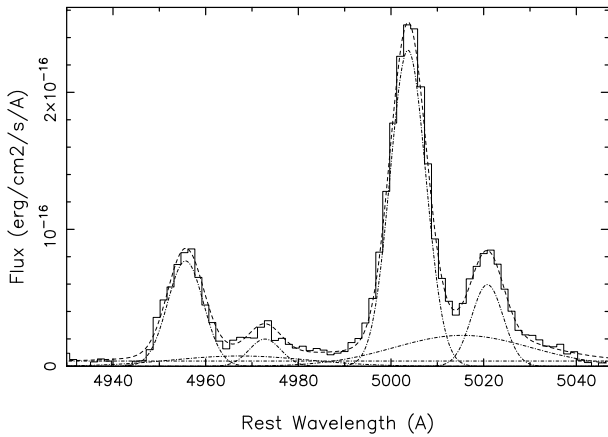


**Figure 2.** [OIII] $\lambda\lambda$ 4959,5007 emission-line profiles (solid line) from the long-slit spectrum:  $1.63 \times 2.16$  arcsec $^2$  aperture centred at 1.5 arcsec SE of the continuum centroid. The multicomponent Gaussian fits (dot-dashed-dot lines) and the total fit (dashed line) are also plotted.

a better fit than the three narrow components suggested by Tadhunter (1991). The velocity shifts of the three components are given with respect to the velocity at the continuum centroid. The low- and high-velocity components have linewidths close to the spectral resolution limit.

#### 4.1.2 Emission-line spectra

Integrated spectra of five spatial regions along the slit for 3C 265, together with a two-dimensional spectrum showing the [OIII] $\lambda\lambda$ 4959,5007 doublet, are presented in Fig. 1. The integrated fluxes of the observed emission-lines in these regions, normalized to the corresponding observed-frame H $\beta$  flux, are given in Table 2. The line ratios have not been corrected for intrinsic reddening, given that the intensities of H $\delta$  and H $\gamma$  relative to H $\beta$  are not significantly lower than expected for Case B recombination (Osterbrock 1989), suggesting that the intrinsic reddening is not large.

## 4.2 Optical imaging

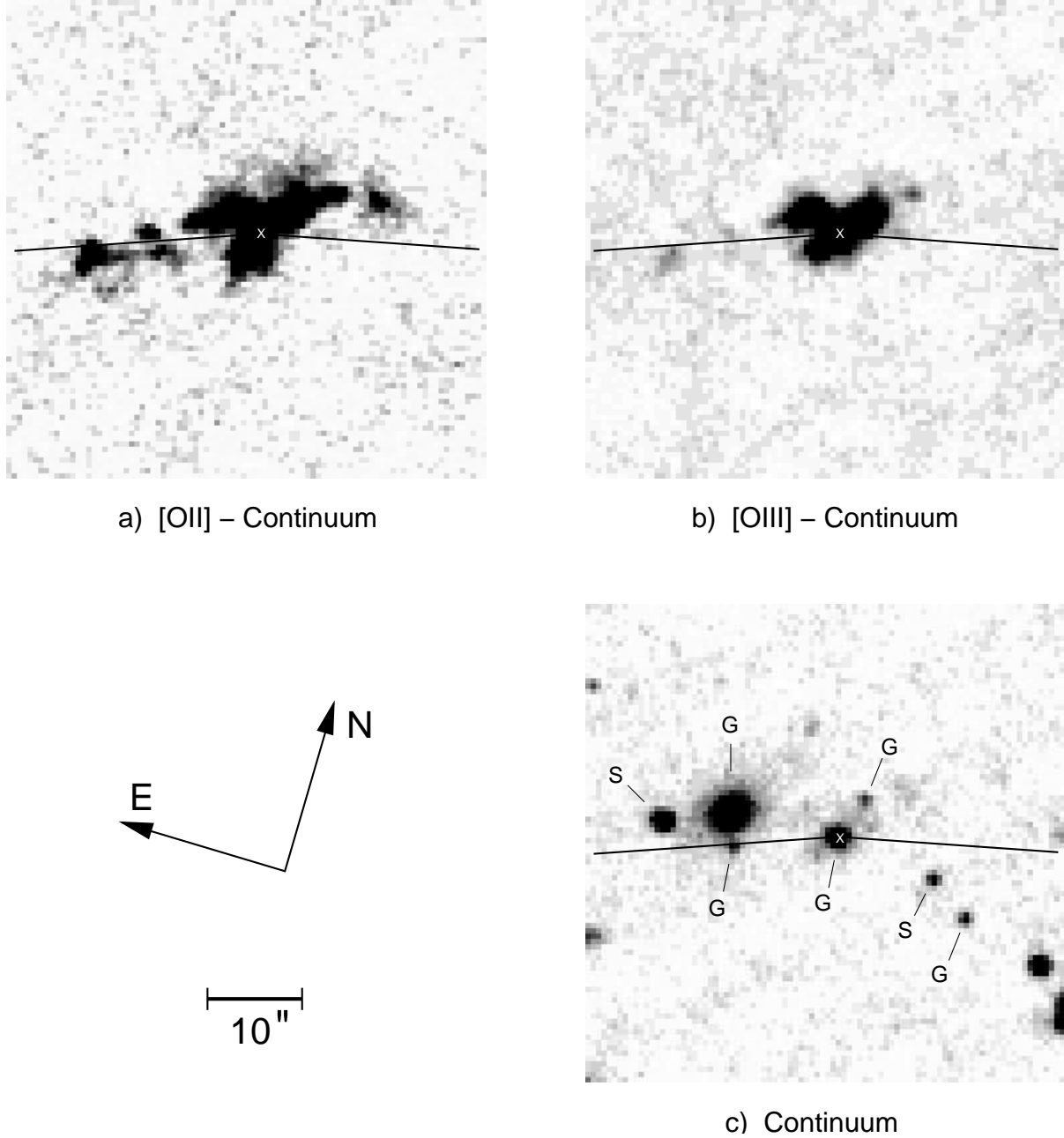


**Figure 3.** TTF images of 3C 265: a) [OII] $\lambda\lambda 3727$  emission-line image for the low-velocity component; b) [OIII] $\lambda 5007$  emission-line image for the low-velocity component; c) Continuum image centred on (rest-frame) 4485 Å. On the basis of examination of high resolution HST images, the objects detected in the continuum image (c) have been classified into galaxies (G) and stars (S). All three images cover 50.13 arcsec (414 kpc) in both directions. The galaxy continuum centroid is indicated by a white ‘x’, and the solid line represents the radio axis.

#### 4.2.1 Emission-line and continuum structures

Fig. 3 presents deep [OII] $\lambda\lambda 3727$ , [OIII] $\lambda 5007$  and continuum images of 3C 265, showing the spectacular emission structure of this object. The galaxy continuum centroid is indicated by a white ‘x’, and the solid lines represent the axes of the large scale radio emission on either side of the nucleus (Fernini et al. 1993).

Image (a) shows the continuum-subtracted [OII] emission-line structure for the low-velocity component. Before the continuum subtraction, the continuum image was

scaled to the [OII] image according to the corresponding bandwidths of the broad-band filter and etalon, respectively. It can be seen that the emission extends over more than 35 arcsec (290 kpc) across the galaxy, confirming previous results presented by Rigler et al. (1992) and McCarthy, Spinrad & van Breugel (1995). On the eastern side of the galaxy the [OII] emission extends up to approximately 20 arcsec (165 kpc) from the centre of the galaxy, and is closely aligned along the radio axis on a large scale, between 10 and 20 arcsec (82 – 165 kpc) from the nucleus. However, closer to the

nucleus, no clear alignment can be observed between the emission and radio structures. In fact, within a radius of 10 arcsec the highest surface-brightness [OII] emission appears to be misaligned by  $\sim 30 - 40^\circ$  with respect to the radio axis. Note also the presence of significant flux perpendicular to the radio axis in the central regions ( $r \lesssim 7$  arcsec; 58 kpc).

Of particular interest is the ‘hole’ in the emission structure located between 10 and 12 arcsec (82 – 100 kpc) along the radio axis on the eastern side of the nucleus. Note the remarkable coincidence of the hole lying exactly on the radio axis, suggesting that it is due to the passage of the radio jet through the cloud. Faint linear features can also be noticed along the radio axis at  $\sim 13$  arcsec (107 kpc) to the east of the nucleus, and possibly at  $\sim 7$  arcsec (58 kpc) to the west of the nucleus.

The continuum-subtracted [OIII] emission-line structure for the low-velocity component is presented in image (b). The continuum subtraction was performed in the same way as for the [OII] image. The emission structure in [OIII] is much more centrally concentrated than the [OII] structure (this is not due to the relative depth of the images). The high-surface-brightness structures do not show a clear alignment with the radio axis. Only a faint [OIII] emission region can be seen along the radio axis,  $\sim 18$  arcsec (150 kpc) to the east of the nucleus. There are indications that the possible linear feature observed in the [OII] image at  $\sim 7$  arcsec (58 kpc) to the west of the nucleus, may be also detected at the same location along the radio axis in the [OIII] structure.

It can be seen that the [OII] and [OIII] emission-line structures are consistent with a large ( $\sim 60^\circ$ ) half-opening angle for the ionization bicone predicted by the unified schemes. However, in both images, significant flux is also detected outside the cones, perpendicular to the radio axis, in the nuclear regions. Note also the apparent ‘hollowing out’ of the cones, which could be the result of outflows induced by the central AGN. A similar edge-brightened biconical structure is seen on a much smaller scale in Cygnus A (Tadhunter et al. 1999).

Image (c) shows the continuum emission of 3C 265. The central (rest-frame) wavelength of the filter was 4485 Å, with a bandwidth of 330 Å. Therefore, any important emission-line contamination was avoided. This image shows a central compact galaxy, with a companion galaxy at 5 arcsec (41 kpc) to the north-north-west, which is also detected in infrared images (Best, Longair & Röttgering 1997) and presents colours consistent with the same redshift as 3C 265 (Best, private communication). The bright galaxy at 12 arcsec to the east of 3C 265 is a foreground elliptical galaxy at redshift  $z=0.392$  (Smith et al. 1979). There is also a faint galaxy at  $\sim 11$  arcsec (90 kpc) to the east of the nucleus, coincident with the emission-line structures aligned along the radio axis. The colours of this galaxy do not give an unambiguous estimate of its redshift: it could be either at the redshift of 3C 265 or at the redshift of the brighter foreground elliptical galaxy (Best, private communication).

#### 4.2.2 Emission-line kinematics: high-velocity gas

As mentioned above (Section 4.1.1), we find that the kinematic structure of 3C 265 to the south-east of the nucleus

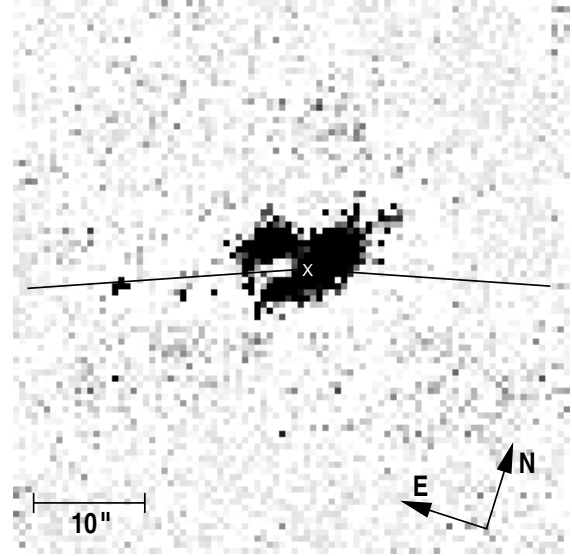


**Figure 4.** Image of 3C 265 showing the ratio between the low- and the high-velocity components to the [OIII]λ5007 emission line. The high-velocity gas is represented by white. The continuum centroid is indicated by a ‘x’, and the solid line represents the radio axis. Note the close alignment between the high-velocity cloud to the east of the nucleus, and the radio axis.

along PA  $145^\circ$ , can be resolved into three components: two narrow split components, moving at  $-222$  and  $+800$   $\text{km s}^{-1}$  relative to the continuum centroid, and a very broad component with a velocity shift of  $+500$   $\text{km s}^{-1}$ . Our new TTF images provide more information about the location of the  $+800$   $\text{km s}^{-1}$  high-velocity cloud.

In Fig. 4 we show the ratio between the low- ( $-222$   $\text{km s}^{-1}$ ) and the high- ( $+800$   $\text{km s}^{-1}$ ) velocity filter images for the [OIII]λ5007 emission line. The high-velocity gas is represented by white, and black indicates where the low-velocity component dominates. The solid line represents the radio axis and the continuum centroid is indicated by a ‘x’. Although the wavelength overlap in the Lorentzian profiles of the TTF at the two etalon settings precludes the determination of an accurate flux ratio for the high- relative to the low-velocity component, this image does allow the spatial position of the high-velocity component to be determined accurately.

We find that the high-velocity cloud has a spatial extent of  $(1.7 \pm 0.3) \times (2.2 \pm 0.3)$  arcsec<sup>2</sup> ( $14 \times 18$  kpc<sup>2</sup>) and is centred at  $2.46 \pm 0.13$  arcsec (20 kpc) SE of the continuum centroid of the galaxy, along PA  $101.9^\circ \pm 2.0^\circ$ . Given that the radio axis is along PA  $112.0^\circ \pm 0.5^\circ$  on the eastern side of the radio core (see Fernini et al. 1993 for radio map), we find that the centroid of the high-velocity cloud is located at a (perpendicular) distance of  $0.43 \pm 0.09$  arcsec (3.5 kpc) north from the radio axis, subtending from the galaxy continuum centroid an angular offset of  $10.1^\circ \pm 2.0^\circ$  from the radio axis on the eastern side of the nucleus. This close alignment strongly suggests that the high-velocity gas is associated with the radio jet axis.

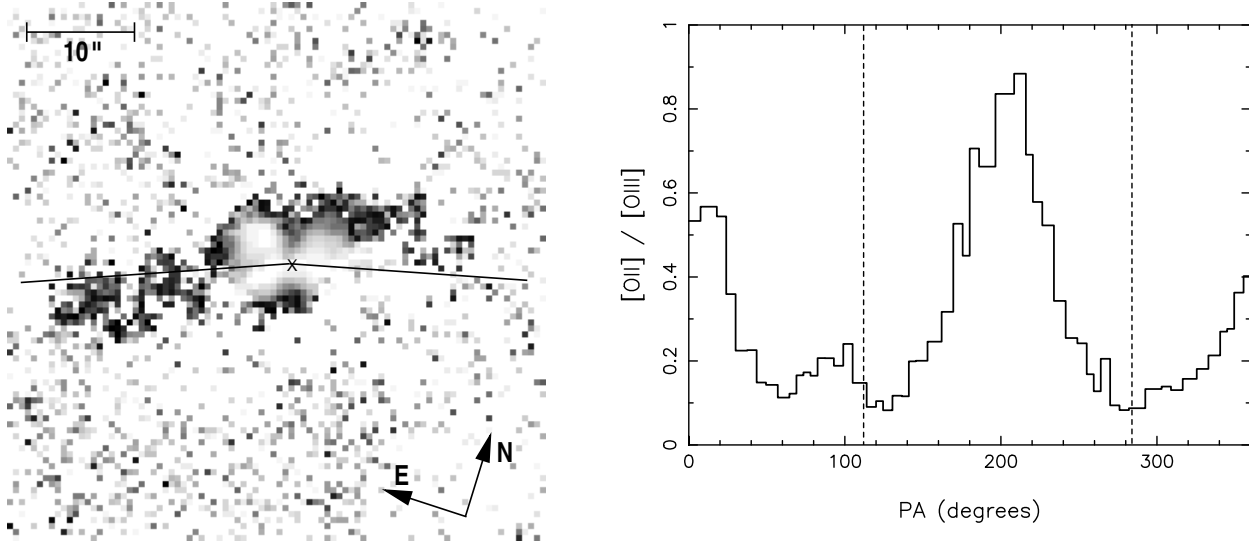


**Figure 5.** Left: Image of 3C 265 showing the  $[\text{OII}]\lambda 3727 / [\text{OIII}]\lambda 5007$  line ratio for the low-velocity component. White indicates high ionization, and black indicates low ionization. The continuum centroid and the radio axis are indicated by a ‘x’ and a solid line, respectively. Right: Azimuthal profile of the line ratio  $[\text{OII}]/[\text{OIII}]$  in 3C 265 (evaluated between 2.23 and 3.34 arcsec distance from the nucleus). The vertical dashed lines represent the radio axes.

#### 4.2.3 Ionization

An ionization map of 3C 265 is shown in Fig. 5 (left). This image is the ratio between the  $[\text{OII}]\lambda 3727$  and the  $[\text{OIII}]\lambda 5007$  images, for the low-velocity component. White indicates high ionization, and black corresponds to low ionization. The continuum centroid and the radio axis are indicated, as in previous figures, by a ‘x’ and a solid line, respectively.

The ionization state of the nucleus is high, and decreases with radius from the centre. At radii smaller than 7 arcsec (58 kpc) from the centre, the ionization structure has a ‘butterfly’ shape, which is consistent with a bicone of  $60^\circ \pm 10^\circ$  half-opening angle, predicted by the unified schemes. Within the bicone, the ionization decreases near the edges, and keeps decreasing in the regions lying outside it. Note the presence of low-ionization material located perpendicular to the radio axis, about 4 arcsec (33 kpc) to the north and south of the nucleus.

Fig. 5 (right) shows the azimuthal profile of the line ratio  $[\text{OII}]/[\text{OIII}]$ , extracted from the ionization map and evaluated between 2.23 and 3.34 arcsec (18 – 28 kpc) distance from the nucleus. The vertical dashed lines represent the radio axis. This plot shows how strongly the ionization of the emission-line gas varies as a function of position angle. A very strong change in the ionization ratio is apparent moving away from the radio axis, showing clear evidence for ionization cones with half-opening angle of  $\sim 50^\circ - 65^\circ$ . The ionization state within the cones is high ( $0.1 \lesssim [\text{OII}]/[\text{OIII}] \lesssim 0.3$ ), and decreases sharply towards the edges. It can be seen that gas with lower ionization state is present outside the cones around the position angles  $20^\circ$  and  $200^\circ$ , with line ratios of  $[\text{OII}]/[\text{OIII}] \simeq 0.5$  and  $[\text{OII}]/[\text{OIII}] \simeq 0.8$ , respectively. It is striking that the low-ionization peaks are separated by  $\sim 180^\circ$ , and the radio axes on either side of the nucleus are roughly mid way between the peaks.

On the other hand, as we move to larger distances from

the central region, the ‘butterfly’ shape in the ionization map vanishes, and only low-ionization emission regions can be seen in the structure. The low-ionization gas extends up to 15 arcsec (124 kpc) to the north-west and, on the eastern side, is closely aligned along the radio axis, extending up to a radius of  $\sim 24$  arcsec (200 kpc).

In addition, Fig. 5 resolves the long-standing issue concerning the optical/UV misalignment with the radio axis in 3C 265. Dey & Spinrad (1996) suggested that this misalignment may be due to a misalignment between the axis of the quasar illumination cone and the radio axis, which would have important implications for the understanding of AGN. However, 3C 265 clearly possesses a broad ( $\sim 60^\circ$  half-opening angle) ionization cone, aligned with the radio axis, and therefore the optical/UV misalignment must be due to the intrinsic matter distribution.

## 5 DISCUSSION

### 5.1 The dominant ionization mechanism

As discussed in the introduction, spectroscopic and polarimetric studies provide clear evidence for AGN-illumination in the extended gas of 3C 265 (e.g. di Serego Alighieri et al. 1996). This is also supported by a more recent analysis of the ionization state of the extended gas of 3C 265, based on long-slit spectroscopic observations, which shows that the near-UV emission-line ratios are consistent with photoionization by the central active nucleus (Best et al. 2000).

Our results reinforce the evidence for AGN illumination in the central regions of 3C 265. The  $[\text{OII}]\lambda 3727$  and  $[\text{OIII}]\lambda 5007$  images, presented in Fig. 3, show that the main central structure is elongated along PA  $145^\circ$ , and misaligned with the radio axis by approximately  $40^\circ$ . The emission-line structure is consistent with anisotropic illumination by the quasar which illuminates the ambient gas within the pre-

dicted ionization cones. In this case, the cones are edge-brightened with a large ( $\sim 60^\circ \pm 10^\circ$ ) half-opening angle. Further evidence for anisotropic illumination is given by the ionization map presented in Fig. 5, which shows the ‘butterfly’ shape of the ionization structure in the central region, suggesting the existence of the predicted cones. The high ionization state of the gas within the cones is also clear from this image.

We noted in the previous section the presence of gas outside the putative ionization cones, perpendicular to the radio axis on both sides of the nucleus, and our line ratio map shows that it has a low ionization state [see Fig. 5 (left)]. The nature of this emission-line gas cannot be explained in terms of anisotropic illumination from the central active nucleus, but other possibilities can be considered. These include: ionization by some back-scattered light from within the cones; photoionization by stars; shock-ionization as a result of the interactions between streams of gas during a merger or accretion event (Koekemoer 1994); and shock-ionization due to the lateral expansion of the radio cocoon.

Moving to larger distances from the nucleus ( $>10$  arcsec; 80 kpc), the [OII] emission-line structure is much more tightly aligned with the radio axis [see Fig. 3 (a)], which is not expected on the basis of illumination by the broad radiation cones predicted by the unified schemes (Barthel 1989). On this scale, the close alignment and high collimation of the structure is similar to that observed in objects like 3C 266, 3C 324 and 3C 368, in which shock-ionization is suspected (Best et al. 2000). Indeed, such close alignment of low-ionization gas with the radio axis is in agreement with the jet-cloud interaction model. The passage of the radio jet drives strong shocks into the clouds, which are compressed, ionized and heated; the density of the clouds will increase resulting in a lower ionization parameter. As the post-shock clouds cool, line radiation will be emitted, particularly strongly in the low-ionization lines. Detailed studies of nearby radio galaxies with jet-cloud interactions revealed a large [OII]/[OIII] line ratio in the shocked regions (Clark et al. 1997, 1998; Villar-Martín et al. 1999).

The importance of jet-cloud interactions in the very extended gas of 3C 265 is also supported by the detection of a ‘hole’ in the [OII] extended structure, lying close to the radio axis, about 11 arcsec (90 kpc) to the east of the nucleus [see Fig. 3 (a)], suggesting that this is due to the passage of the radio jet through the cloud; and also by the presence of faint linear features along the radio axis, at 13 arcsec (107 kpc) east from the nucleus in the [OII] image, and possibly at 7 arcsec (58 kpc) west from the nucleus in both [OII] and [OIII] images [see Fig. 3 (a) and (b)].

Overall, these results indicate that the ambient gas in 3C 265 is mainly ionized by the central active nucleus at relatively small distances ( $\lesssim 7$  arcsec; 58 kpc) from the centre of the galaxy. However, the situation at larger radii is less clear. Because of the  $r^{-2}$  fall off in the nuclear radiation field, we would expect jet-induced shocks to be relatively more important on a large scale. This is supported by the close alignments observed on this scale; but high-resolution kinematic studies are required to test the idea that this gas has indeed undergone a jet-cloud interaction, by searching for the expected kinematic signatures of such interactions. Unfortunately, the existing spectroscopic studies of McCarthy,

Baum & Spinrad (1996) of that region, are not of sufficient quality for this purpose.

Something similar is seen in low-redshift starburst galaxies, where photoionization from the central starburst source dominates in the inner regions, and the importance of shock-ionization increases at larger radii (Shopbell & Bland-Hawthorn 1998).

These results also demonstrate that the alignment effect can be important on a large scale, even in cases in which the alignment is poor on a smaller scale and in which the radio structure extends much further than the emission-line structures.

### 5.1.1 Emission-line ratios

To study in more detail the ionization mechanism of the line-emitting gas, we have compared the emission-line ratios for different regions in 3C 265 with theoretical predictions of both AGN-photoionization and shock-ionization models. The diagnostic diagrams are presented in Fig. 6, and include the following line ratios: (a) [OIII](5007)/H $\beta$  vs. [OII](3727)/[OIII](5007); (b) [OIII](5007)/H $\beta$  vs. [NeV](3426)/[NeIII](3869); and (c) [OII](3727)/[OIII](5007) vs. [NeV](3426)/[NeIII](3869).

The measured line ratios were derived from the long-slit spectra along PA  $145^\circ$ . The points correspond to the five spatial regions defined along the slit (see Section 4.1.2 for details). Note that the slit was misaligned by  $\sim 35^\circ$  with respect to the radio axis.

The data are compared with various ionization models which include: power-law photoionization (solid lines), photoionization including matter-bounded clouds (dot-dash-dot line), and shocks including a photoionized precursor (dotted lines). Note that simple shock cooling zone models (i.e. without a precursor region) lie outside the diagrams. To generate the different ionization model predictions we followed the same procedure described in Solórzano-Iñarrea et al. (2001), to which the reader is referred for further references and details.

By comparing the three diagnostic diagrams, we see that all of the points fall well away from the ‘pure’ shock models and within the region occupied by the photoionization predictions, although there is not complete consistency between the diagrams. Note, however, that this inconsistency does not rule out AGN-photoionization because the models — particularly the mixed-medium models — could be tuned to improve the fits in the diagrams. Similar problems of inconsistency, when comparing line ratios with ionization model predictions, have been found for other high-redshift radio galaxies (Solórzano-Iñarrea et al. 2001). In the case of the outer EELR (small filled squares), shock+precursor predictions with magnetic parameter  $B/\sqrt{n} = 0 \mu\text{Gcm}^{-3/2}$  and shock-velocity in the range  $400 \leq v_s \leq 500 \text{ km s}^{-1}$  could also give a reasonable fit to those regions; but in all other regions the line ratios appear more consistent with AGN-photoionization.

Note that the nucleus (star) and the low-velocity component (filled circle) overlap each other in the three diagrams, which indicates that these two regions have a similar ionization state. In contrast, the high-velocity component (open circle) occupies a different region in the diagrams, with the highest ionization among all regions, although the

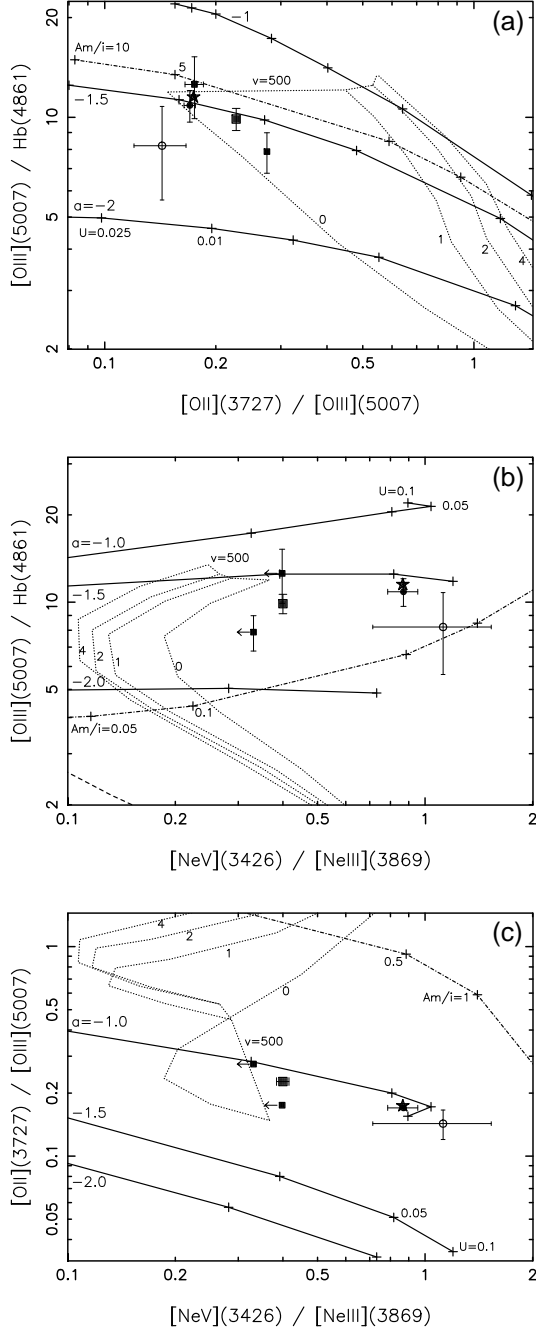


**Figure 6.** Diagnostic diagrams for different regions of 3C 265, including: nuclear region (star), inner SE EELR showing both low- (filled circle) and high- (open circle) velocity components, inner NW EELR (big filled square), and outer SE and NW EELR (small filled squares). Solid lines represent optically-thick power-law ( $F_\nu \propto \nu^\alpha$ ) photoionization models (from MAPPINGS) with  $\alpha = -1.0, -1.5$  and  $-2.0$ , and a sequence in the ionization parameter ( $2.5 \times 10^{-3} < U < 10^{-1}$ ). The dot-dash-dot line corresponds to photoionization models including matter-bounded clouds ( $10^{-2} \leq A_M/I \leq 5$ ) from Binette, Wilson & Storchi-Bergmann (1996). The dotted lines represent shocks+precursor models from Dopita & Sutherland (1995, 1996), each sequence corresponds to a fixed magnetic parameter ( $B/\sqrt{n} = 0, 1, 2, 4 \mu\text{Gcm}^{-3/2}$ ) and a changing shock velocity ( $150 \leq v_s \leq 500 \text{ km s}^{-1}$ ). Note that simple shock predictions (without a precursor) lie outside the diagrams.

errors for this component are also bigger than for the other points.

### 5.1.2 High-velocity gas

It seems clear that at small nuclear distances ( $\lesssim 7 \text{ arcsec}$ ) the main ionization mechanism is photoionization by the central quasar. However, high-velocity gas is detected at  $\sim 2.5 \text{ arcsec}$  (20 kpc) from the centre of 3C 265 (see Section 4.2.2), within the ionization cone, where the effects of AGN illumination should dominate. The projected velocity of the fast-moving cloud with respect to that of the surrounding gas is approximately  $1000 \text{ km s}^{-1\dagger}$ . Such a large velocity amplitude cannot be caused by gravity of a single galaxy (Tadhunter et al. 1989), but could be explained in terms of acceleration by the interaction with the radio structures. Tadhunter (1991) suggests that such large velocity shifts are due to cocoons of material expanding around the radio jets, perhaps remnants of the bow-shocks associated with the passage of the jet. This is strongly supported by the location of the high-velocity cloud, which lies close to the radio axis (see Fig. 4). Although acceleration by AGN- or starburst-induced winds could be considered as an alternative mechanism (e.g. Heckman, Armus & Miley 1990), such winds would be expected to produce a broad outflow right across the cone, and not localised on the radio axis.

It is surprising that a galaxy such as 3C 265, in which the radio source is on a much larger scale than the emission-line structures, presents signs of jet-cloud interactions. However, 3C 265 is not the only large radio source in which these interactions have been detected. Kinematic evidence for shock-acceleration has been also found in two other high-redshift radio galaxies (3C 34 and 3C 330), in which the radio hot spots have passed well beyond the EELR (Solórzano-Iñarrea et al. 2001).

Although the high-velocity cloud may have been shock-accelerated, that does not necessarily mean that the cloud is shock-ionized. It could be accelerated by jet-induced shocks but still photoionized by the central active nucleus. In either case, if we believe the high-velocity cloud to be accelerated as a result of the interaction with the radio structures, the density of the cloud will increase because of the compression effect of the shocks (a factor of 10 to 1000; e.g. Begelman & Cioffì 1989; Komissarov 1994), and therefore a lower ionization parameter than that of the surroundings is expected. However, as discussed in the previous section, this is not observed. The high-velocity gas appears to have similar, if not higher, ionization state than the emission-line regions in the vicinity.

If the high-velocity gas is actually the result of the interaction with the radio components, then how can we explain the high-ionization state and narrow linewidths observed in the line-emitting gas? Assuming that the regions behind the shock front are destroyed, we would expect to measure weaker low-ionization emission lines, which are emitted mainly by the cooling post-shock clouds, resulting in a higher-than-expected observed ionization state. Thus,

<sup>†</sup> Note that if the high-velocity cloud is undergoing radial motion close to the plane of the sky, the *deprojected* radial velocity of the cloud could be much larger.

‘matter-bounded shocks’, previously considered for high-redshift radio galaxies (Solórzano-Iñarrea et al. 2001), could be another possible explanation for the high-velocity cloud in 3C 265.

Alternatively, since the cloud lies close to the direction of the radio axis, it could fall within the narrow cone ( $\lesssim 10^\circ$  half-opening angle) defined by the blazar beam of the relativistic jets. The higher ionizing flux density of the beam — about an order of magnitude greater than that of the unbeamed component (Browne & Murphy 1987) — might dominate over the compression effect of the shocks, therefore increasing the ionization state of the high-velocity cloud. However, given that the compression across a strong radiative shock could be a factor of  $>100$  (e.g. Begelman & Cioffi 1989; Komissarov 1994), it is not clear that the boost in ionizing flux density due to the blazar beam would be enough to produce the high ionization state in the high-velocity gas.

It is notable that kinematic disturbed components with high ionization state have been detected in the nuclear regions of several other objects, including the extended radio source Cygnus A (Tadhunter 1991), and the compact radio sources PKS 1549-79 (Tadhunter et al. 2001), PKS 1345+12 (Grandi 1977) and 3C 48 (Chatzichristou, Vanderriest & Jaffe 1999). These three latter sources present high-ionization emission lines that are unusually broad and shifted relative to the low-ionization emission lines. In the case of Cygnus A, a high-velocity component, with similar or higher ionization state than the unshifted component, is detected at  $\sim 1$  arcsec (1.5 kpc) NW of the radio core and located close to the radio axis, just like 3C 265 (Tadhunter 1991; Tadhunter, Metz & Robinson 1994; Stockton, Ridgway & Lilly 1994).

In contrast with these sources, detailed studies of the jet-cloud interactions on a larger scale (20 – 50 kpc) in the powerful radio galaxy PKS 2250-41 have revealed multi-component emission-line kinematics: a low-ionization broad component, representing material cooling behind the shock front; and a high-ionization narrow component, which represents the AGN- or shock-photoionized precursor gas (Villar-Martín et al. 1999). Our long-slit spectra of 3C 265 reveal relatively narrow linewidths ( $<250 \text{ km s}^{-1}$ ) for the high-velocity emission-line gas, similar to those of the low-velocity component (see Section 4.1.1). However, in this case, unlike for PKS 2250-41, the narrow high-velocity component cannot represent the photoionized precursor gas, given the high velocity of  $\sim 1000 \text{ km s}^{-1}$  at which the cloud is moving relative to the surrounding gas.

Overall, the existence of fast-moving gas along the radio axis with higher ionization states than the surrounding emission-line gas remains a mystery. No explanation for the high ionization state seems entirely satisfactory, and further investigation is required for this issue.

## 5.2 Intrinsic gas structure

3C 265 is an extreme radio galaxy in terms of luminosity, morphology and emission-line properties. Its bizarre optical morphology, completely surrounded by emission regions and companion galaxies, revealed by HST images, suggests that 3C 265 is undergoing the process of merging (Longair, Best & Rottgering 1995). More recent analysis of the environment around 3C 265 show that there are indeed companion

galaxies surrounding 3C 265, and reveal that the galaxy lies in a cluster environment (Best 2000).

The continuum image, presented in Fig. 3 (c), shows that the closest companion galaxy, to the north-north-west of 3C 265, aligns along the axis of the highest surface brightness [OII], [OIII] and UV-continuum emission elongation (PA  $\sim 150^\circ$ ). In Section 4.2.3 it was shown that the ionization cone of the AGN in 3C 265 is indeed aligned with the radio axis, therefore the optical/UV emission elongation must be intrinsic, since there is no reason why the gas would not be illuminated symmetrically. This suggests that the gas and dust present along the position angle of the optical/UV elongation may be associated with an interaction/merger involving 3C 265 and this companion. Moreover, both the increase of the covering factor due to the extra amount of gas along this direction, and the fact that 3C 265 is among the most powerful radio sources known (e.g. Laing, Riley & Longair 1983) may explain why its emission-line luminosity is so extreme.

It is also intriguing that the next closest galaxy in terms of projected distance from the nucleus — 11 arcsec (90 kpc) to the east of the nucleus — is aligned with the PA of the large scale ( $\gtrsim 9$  arcsec; 75 kpc) gas on both sides of the nucleus (PA  $\sim 120^\circ$ ). If more detailed observations demonstrate that this is a genuine companion galaxy, then it is plausible that the larger scale emission-line structure also represents a gas stream associated with a merging companion. In this case, the large scale elongation in the gas distribution along the radio axis may be intrinsic, rather than a consequence of jet-cloud interactions.

Similarly, images of other powerful radio galaxies reveal companion galaxies aligned along the direction of the aligned optical/UV emission. Examples include: 3C 65, 3C 266, 3C 324, 3C 356 and 3C 368 (Dunlop & Peacock 1993; Best et al. 1996, 1997).

This suggests that the highest surface brightness structures in radio galaxies may be aligned along a preferred direction, defined by mergers with companion galaxies. This is in agreement with the idea proposed by West (1994), who suggests that powerful radio galaxies at high redshifts are formed by a hierarchical, highly-anisotropic merging processes.

## 6 CONCLUSIONS

We report the results from a study of the morphology, kinematics and ionization structure of the powerful radio galaxy 3C 265.

Our results show that different ionization mechanisms may dominate on different scales. We find that close to the nucleus the dominant ionization mechanism is AGN-photoionization. This is supported by the detection of the broad ionization cones predicted by the unified schemes. In contrast, as we move to large distances from the nucleus, jet-cloud interactions become the main ionization mechanism of the line-emitting gas, and the gas appears more closely aligned with the radio axis. The presence of a high-velocity cloud, located close to the passage of the radio jet and centred at approximately 2.5 arcsec (20 kpc) from the nucleus, shows that the effects of jet-induced shocks are still important in the nuclear regions. However, it is particularly

puzzling that this fast-moving gas presents a high ionization state; if the cloud is believed to have been shock-accelerated, it would be expected to have lower ionization state than the surroundings, but this is not observed. Clearly, more data are required to investigate this issue.

In addition, our results suggest that the intrinsic distribution of the gas close to the nucleus ( $\lesssim 60$  kpc) in 3C 265 is aligned along a preferred direction (misaligned with the radio axis), which may be the result of a highly-anisotropic merging process. On the other hand, at large distances from the nucleus, where jet-cloud interactions dominate, the low-ionization emission-line regions align along the direction of the radio axis.

Overall, our results demonstrate that a combination of mechanisms is required in order to explain the observed properties of the line-emitting gas in the haloes of radio galaxies. This confirms our previous results presented in Solórzano-Iñarrea et al. (2001), which show evidence for shock-acceleration in the EELR of all the galaxies in a small sample, even those in which the shock fronts have passed the EELR and AGN-illumination would have been expected to dominate.

## ACKNOWLEDGMENTS

This work is based on observations made at the Observatorio del Roque de los Muchachos, La Palma, Spain. The long-slit spectra used for this paper were taken from the ING Archive. We thank Philip Best for reading the manuscript and giving useful suggestions. CSI acknowledges a White Rose studentship. This research has made use of the NASA/IPAC Extragalactic Database (NED) which is operated by the Jet Propulsion Laboratory, California Institute of Technology, under contract with the National Aeronautics and Space Administration. We thank the anonymous referee for helpful comments.

## REFERENCES

- Barthel P. D., 1989, *ApJ*, 336, 606  
 Baum S. A., Heckman T., van Breugel W., 1990, *ApJS*, 74, 389  
 Begelman M. C., Cioffi D. F., 1989, *ApJL*, 345, L21  
 Best P. N., Longair M. S., Röttgering H. J. A., 1996, *MNRAS*, 280, L9  
 Best P. N., Longair M. S., Röttgering H. J. A., 1997, *MNRAS*, 292, 758  
 Best P. N., Röttgering H. J. A., Longair M. S., 2000, *MNRAS*, 311, 23  
 Best P. N., 2000, *MNRAS*, 317, 720  
 Binette L., Wilson A. S., Storchi-Bergmann T., 1996, *A&A*, 312, 365  
 Bland-Hawthorn J., Jones D. H., 1998a, *PASP*, 15, 44  
 Bland-Hawthorn J., Jones D. H., 1998b, *SPIE*, 3355, 855  
 Browne I. W. A., Murphy D. W., 1987, *MNRAS*, 226, 601  
 Chatzichristou E. T., Vanderriest C., Jaffe W., 1999, *A&A*, 343, 407  
 Clark N. E., Tadhunter C. N., Morganti R., Killeen N. E. B., Fosbury R. A. E., Hook R. N., Siebert J., Shaw M. A., 1997, *MNRAS*, 286, 558  
 Clark N. E., Axon D. J., Tadhunter C. N., Robinson A., O’Brien P., 1998, *ApJ*, 494, 546  
 Dey A., Spinrad H., 1996, *ApJ*, 459, 133  
 di Serego Alighieri S., Cimatti A., Fosbury R. A. E., Perez-Fournon I., 1996, *MNRAS*, 279, L57  
 Dopita M. A., Sutherland R. S., 1995, *ApJ*, 455, 468  
 Dopita M. A., Sutherland R. S., 1996, *ApJS*, 102, 161  
 Dunlop J. S., Peacock J. A., 1993, *MNRAS*, 263, 936  
 Ferrini I., Burns J. O., Bridle A. H., Perley R. A., 1993, *AJ*, 105, 1690  
 Grandi S. A., 1977, *ApJ*, , 446  
 Heckman T. M., Armus L., Miley G. K., 1990, *ApJS*, 74, 833  
 Jannuzi B. T., Elston R., 1991, *ApJL*, 366, L69  
 Koekemoer A. M., 1994, in *American Astronomical Society Meeting*. p. 2607  
 Komissarov S. S., 1994, *MNRAS*, 266, 649  
 Laing R. A., Riley J. M., Longair M. S., 1983, *MNRAS*, 204, 151  
 Longair M. S., Best P. N., Röttgering H. J. A., 1995, *MNRAS*, 275, L47  
 McCarthy P. J., Baum S. A., Spinrad H., 1996, *ApJS*, 106, 281  
 McCarthy P. J., van Breugel W., Spinrad H., Djorgovski S., 1987, *ApJL*, 321, L29  
 McCarthy P. J., Spinrad H., van Breugel W., 1995, *ApJS*, 99, 27  
 McCarthy P. J., 1988, PhD thesis, University of California  
 Osterbrock D. E., 1989, *Astrophysics of gaseous nebulae and active galactic nuclei*. Research supported by the University of California, John Simon Guggenheim Memorial Foundation, University of Minnesota, et al. Mill Valley, CA, University Science Books  
 Rigler M. A., Stockton A., Lilly S. J., Hammer F., Le Fevre O., 1992, *ApJ*, 385, 61  
 Shopbell P. L., Bland-Hawthorn J., 1998, *ApJ*, 493, 129  
 Smith H. E., Junkkarinen V. T., Spinrad H., Grueff G., Vigotti M., 1979, *ApJ*, 231, 307  
 Solórzano-Iñarrea C., Tadhunter C. N., Axon D. J., 2001, *MNRAS*, 323, 965  
 Stockton A., Ridgway S. E., Lilly S. J., 1994, *AJ*, 108, 414  
 Tadhunter C. N., Fosbury R. A. E., Quinn P. J., 1989, *MNRAS*, 240, 225  
 Tadhunter C. N., Metz S., Robinson A., 1994, *MNRAS*, 268, 989  
 Tadhunter C. N., Packham C., Axon D. J., Jackson N. J., Hough J. H., Robinson A., Young S., Sparks W., 1999, *ApJL*, 512, L91  
 Tadhunter C. N., Wills K., Morganti R., Oosterloo T., Dickson R., 2001, *MNRAS*, in press  
 Tadhunter C. N., 1991, *MNRAS*, 251, 46P  
 Tadhunter C. N., 2001, in Henney W., Steffen W., Binette L., Raga A., eds, *Proceedings of the “Emission Lines from Jet Flows” Conference held on Mexico*, in press  
 Villar-Martín M., Tadhunter C., Morganti R., Axon D., Koekemoer A., 1999, *MNRAS*, 307, 24  
 West M. J., 1994, *MNRAS*, 268, 79